# Indium Tin-Oxide Wrapped 3D rGO and TiO$_2$ Composites: Development, Characterization, and Enhancing Photocatalytic Activity for Methylene Blue

**Cheng Gong [1], Shiyin Xu [1], Peng Xiao [1], Feifan Liu [1], Yunhui Xu [1], Jin Yang [1], Rui Li [1], Xuan Wang [1], Jun Du [1,2,*] and Hailong Peng [1,2,*]**

[1] School of Resources, Environmental, and Chemical Engineering, Nanchang University, No.999 Xuefu Avenue, Nanchang 330031, China; stokescheng@foxmail.com (C.G.); xsy870260363@163.com (S.X.); pengxiao1118@163.com (P.X.); feifan990827@139.com (F.L.); xyh19990218@139.com (Y.X.); yangjin199501@sina.com (J.Y.); lr18053@163.com (R.L.); chritmas9912@gmail.com (X.W.)

[2] Key Lab of Poyang Lake Ecology and Bio-resource Utilization (Ministry of Education), Nanchang University, No.999 Xuefu Avenue, Nanchang 330031, China

\* Correspondence: dujun@ncu.edu.cn (J.D.); penghailong@ncu.edu.cn (H.P.); Tel.: +86-791-8396-9985 (H.P.)

**Abstract:** A hybrid material of indium tin-oxide (ITO) wrapped titanium dioxide and reduced graphene oxide (ITO-rGO and TiO$_2$) was prepared using a facile hydrothermal technique. TiO$_2$ nanorods were in situ grown on the surface of rGO (rGO and TiO$_2$), and which was then assembled onto ITO substrate layer by layer with formation of a 3D structure. ITO-rGO and TiO$_2$ exhibit low charge transfer resistance at the electrode-electrolyte interface and have good photoresponsive ability. Methylene blue (MB) can be effectively adsorbed and enriched onto ITO-rGO and TiO$_2$ surface. The adsorption kinetics and thermodynamics of ITO-rGO and TiO$_2$ were evaluated, showing that the exothermic and entropy-driven reaction were the main thermodynamic processes, and the Langmuir isotherm was the ideal model for adsorption fitting. Meanwhile, ITO greatly improved degradation of rGO and TiO$_2$ because electrons can be collected by ITO before recombination and MB can easily enter into the 3D structure of rGO and TiO$_2$. The highest photodegradation rate of MB reached 93.40% for ITO-rGO and TiO$_2$ at pH 9. Additionally, ITO-rGO and TiO$_2$ successfully solved the problems of being difficult to recycle and causing secondary pollution of traditional TiO$_2$ catalysts. Therefore, ITO-rGO and TiO$_2$ may be a potential photocatalyst for degrading organic pollutants in water.

**Keywords:** ITO-rGO and TiO$_2$; methylene blue; photocatalysis; adsorption; mechanisms

## 1. Introduction

Recently, photocatalysis have become one of the advanced processes for the degrading organic pollutants in wastewater. Among various semiconductor photocatalytic investigations, due to many advantages of titanium dioxide (TiO$_2$), such as low cost, non-toxicity, and high stability, it has received extensive attention [1–4]. Unfortunately, the application of conventional TiO$_2$ photocatalysts still face lots of drawbacks because of low electrical conductivity [5], wide band gap and high recombination rate of electron-hole pairs [6], difficulty separation, and secondary pollution. Therefore, to overcome these shortages of conventional TiO$_2$ photocatalysts, different hybrid TiO$_2$ materials have been investigated over the past years.

Among these hybrid materials, graphene-based TiO$_2$ have been considered as highly photoactive materials [7–12]. Graphene has been well-known as a good catalyst for optimizing the photocatalytic performance of semiconductors. [12–16]. Reduced graphene oxide (rGO) modified with carboxylic acids, hydroxyl groups, and epoxy groups has obvious advantages such as sensitivity to chemical

doping, species adsorbed or bound, and structural deformation [17]. Nowadays, many researchers have been devoted to preparation of rGO doping $TiO_2$ photocatalysts for improving $TiO_2$ catalyst performance [18,19]. However, there is a clear disadvantage that the intermolecular force between rGO and $TiO_2$ is relatively weak and the way they combine via physisorption or van der Waals forces. [20,21]. Its weak connection can cause difficulties in electronic transmission between the rGO and $TiO_2$. Therefore, finding a strong way to combine is necessary for rGO and $TiO_2$ and the C–Ti bond could be a reliable way through a facile hydrothermal method [22].

As an adsorbent and catalyst, nanomaterials have some obvious shortcomings in suspension adsorption and photocatalytic systems due to their difficult solid-liquid separation, which may cause secondary pollution [19,20]. In order to solve the problem of difficult recycling and tackle dispersion, magnetic nanoparticles are used as a substrate to combine with $TiO_2$ [23]. However, the formation of $Fe^{2+}$ is due to the electrons obtained from $Fe^{3+}$ which will cause the iron to be dissolved in the solution. [24]. Such a photochemical dissolution of $Fe^{3+}$ might cause huge damage to the catalyst. In this study, indium tin-oxide (ITO) has many advantages as a promising material such as a low resistivity, and transparency in the visible region [25,26].

Methylene blue (MB) is the most common contaminant in nature and has been studied by many researchers [27,28]. Soma et al. reported removal of MB by rGO-metal oxide ($TiO_2/Fe_3O_4$) based nanocomposites [29]. Wu et al. prepared of a tough $TiO_2$-rGO-PDMAA nanocomposite hydrogel by one-pot UV photopolymerization for photodegradation of MB [30]. Unfortunately, these catalysts have drawbacks of being difficult to separate and causing secondary pollution. In this study, $TiO_2$ and rGO can be easily recycled and taken out from water after bonding to ITO substrate. However, as far as we know, the adsorption and photocatalytic degradation of MB by ITO-$TiO_2$ and rGO in pollution water have never been reported.

In this study, the indium tin-oxide wrapped 3D rGO and $TiO_2$ composites (ITO-$TiO_2$ and rGO) were prepared using a facile hydrothermal method. $TiO_2$ and rGO have a strong electronic correlation as unpaired π electrons were bonded with unsaturated Ti atoms through the hydrothermal method. ITO-$TiO_2$ and rGO exhibited synergy advantage of adsorption and photocatalysis. The most important is that ITO-$TiO_2$ and rGO can be easily recycled and avoide secondary pollution. Meanwhile, ITO-$TiO_2$ and rGO characterizations of morphology, composition, stability, and photoresponsive property were investigated. The static and dynamic adsorption processes were evaluated for ITO-$TiO_2$ and rGO. Finally, photocatalytic performance and mechanism of ITO-$TiO_2$ and rGO were proposed. This work shows that the combination of rGO and $TiO_2$ can greatly reduce the wide band gap of the composite, which makes the electrons more prone to transition in the case of illumination. The combination of composite materials and ITO substrate provides a novel way of consideration for the preparation of environmentally friendly materials. Compared to a single catalyst, our composite catalysts have higher photocatalytic activity and better photoelectric response.

## 2. Results and Discussion

### 2.1. Construction of ITO-rGO and $TiO_2$

The general preparation procedure of ITO-rGO and $TiO_2$ is shown in Figure 1. GO can easily disperse into water due to many hydrophilic functional groups and can be reduced to rGO by DEG. $TiO_2$ was prepared using PTO as a titanium source under hydrothermal conditions. The presence of PVP hinders the contact between titanium dioxide molecules, thus $TiO_2$ was well dispersed in water solution to form nanorods with smaller particle sizes. $TiO_2$ can be coated by rGO via electrostatic interaction and Ti–C bond. Finally, rGO and $TiO_2$ was assembled onto the ITO substrate layer by layer via the annealing method. rGO and $TiO_2$ showed 3D structure on the ITO substrate with excellent adsorption ability and photocatalytic activity for MB in pollution water. Importantly, ITO-rGO and $TiO_2$ can be easily separated and recycled without secondary pollution.
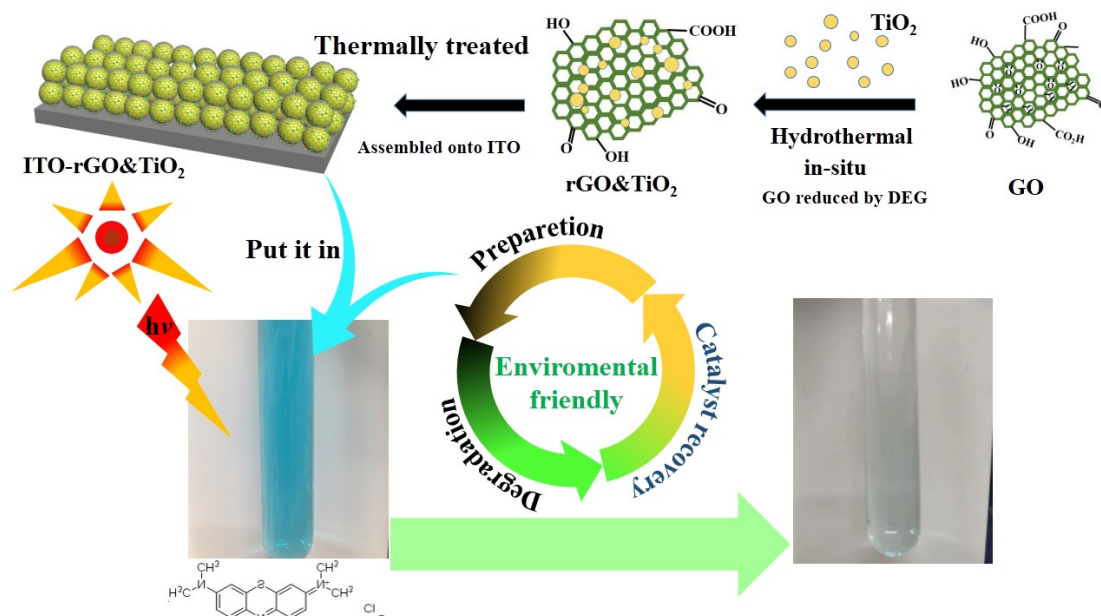
**Figure 1.** The preparation of ITO-reduced graphene oxide (rGO) and titanium dioxide (TiO$_2$) and photocatalytic processes.

*2.2. Characterization of ITO-rGO and TiO$_2$*

2.2.1. XRD

The XRD patterns of different photocatalysts are shown in Figure 2. A strong diffraction peak appeared at 2θ of 10.5°, which correspond to the (001) plane of GO (Figure 2a) [31]. And from XRD pattern of TiO$_2$ and rGO and ITO-TiO$_2$ and rGO, many diffraction peaks appeared at 2θ of 25.307°, 37.792°, 48.043°, 53.886°, 55.068°, 62.689° and 75.051°, which correspond to the (101), (004), (200), (105), (211), (204) and (215) planes of anatase TiO$_2$, respectively. Meanwhile, many diffraction peaks appeared at 2θ of 27.436°, 36.080°, 41.240° according to the XRD standard card (PDF NO. 78–2485), these diffraction peaks correspond to the (110), (101), and (111) planes of rutile TiO$_2$. The XRD results of the pure TiO$_2$ showed that the diffraction peaks all belonged to the anatase phase. However, TiO$_2$ contained two phases of anatase and rutile after coating with rGO.

Figure 2b shows the XRD of ITO-TiO$_2$ and rGO prepared at different reaction times. The diffraction peaks were located at 2θ of 25.307°, 37.792°, 48.043°, and 53.886°, which correspond to the (101), (004), (200), and (105) planes of anatase TiO$_2$, respectively. These diffraction peaks significantly enhanced with increased reaction time, and new diffraction peaks appeared at 2θ of 27.436°, 36.080°, and 41.240°, which corresponded to the (110), (101), and (111) planes of rutile TiO$_2$. Thus, anatase and rutile phase of TiO$_2$ were also present in ITO-TiO$_2$ and rGO. The diffraction peak intensity of TiO$_2$ became stronger with increasing reaction time. Both types of diffraction peaks constantly became stronger under solvothermal condition in the presence of GO. Figure 2c shows the XRD of samples prepared by different DEG concentrations after reaction for 7 h. We can see that the XRD diffraction peaks are the same XRD diffraction peaks when DEG concentration was 3–7 mol/L. However, the diffraction peaks at 2θ of 27.436°, 36.080°, and 41.240° disappeared when DEG was 9 mol/L, which shows that TiO$_2$ has only one crystal form of anatase phase.
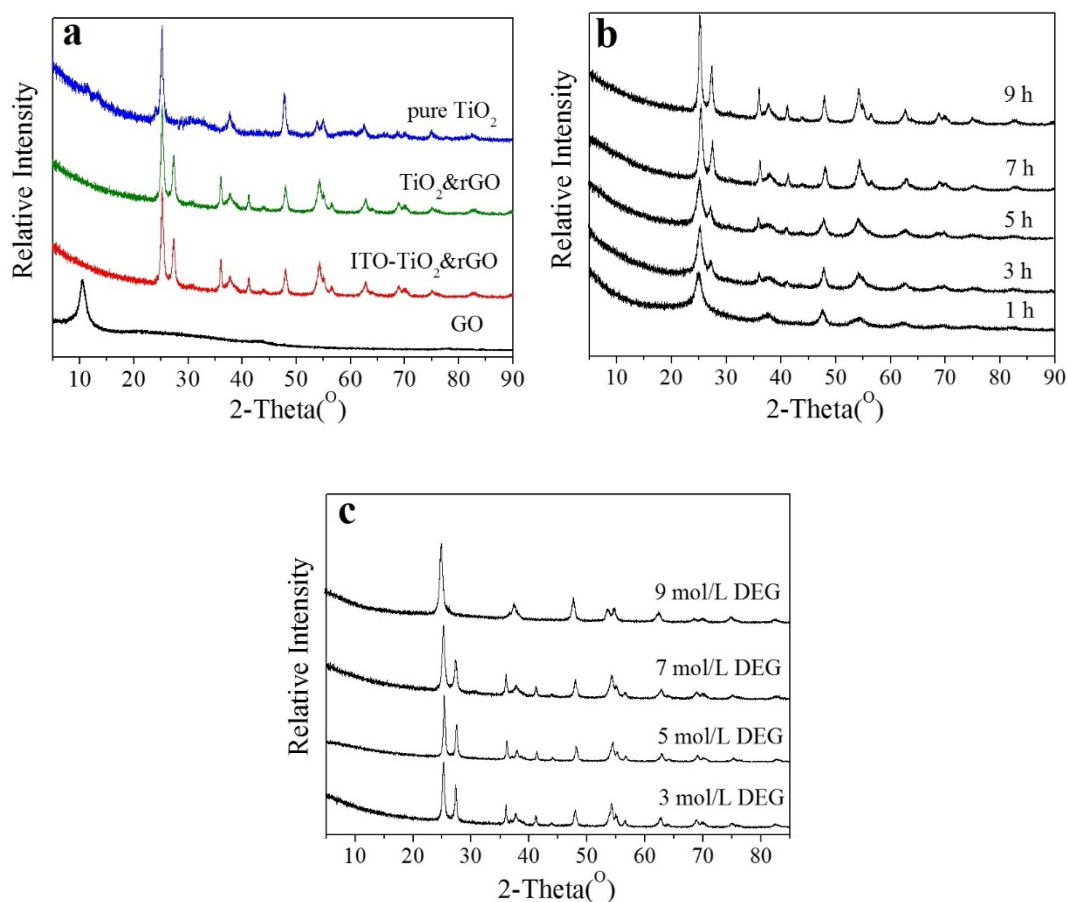
**Figure 2.** X-ray diffractometry (XRD) patterns of (**a**) $TiO_2$, rGO and $TiO_2$, and ITO-rGO and $TiO_2$, (**b**) ITO-rGO and $TiO_2$ prepared at different times, and (**c**) ITO-rGO and $TiO_2$ prepared in different diethylene glycol (DEG) concentrations.

## 2.2.2. SEM

To understand the formation mechanism of ITO-$TiO_2$ and rGO during hydrothermal treatment, the morphology of ITO-$TiO_2$ and rGO was investigated using SEM. Figure 3a shows that GO exists in the form of a sheet. The morphology of pure $TiO_2$ represented nanorods (Figure 3b) and the length and diameter were approximately 0.8 μm and 20 nm, respectively. A previous report indicated that microsphere $TiO_2$ were easily formed due to the aggregation of $TiO_2$ nanoparticles to reduce the surface energy in the hydrothermal treatment under presence of PTO [32]. Meanwhile, the morphologies of ITO-$TiO_2$ and rGO were investigated under different hydrothermal times. The nanorods were not observed when the reaction time was shorter than 3 h (Figure 3c). In addition, some $TiO_2$ nanorods can be seen on the rGO surface after 5 h reaction. When the reaction time reached 7 h, the rGO was completely wrapped by $TiO_2$ nanorods owing to the strong force between $TiO_2$ and rGO. However, $TiO_2$ nanorods on the rGO surface were connected together due to the increase in diameter of the nanorods when the reaction time reached 9 h, which leads to the specific surface area decrease.

Meanwhile, the morphology of ITO-$TiO_2$ and rGO was also investigated when the variable factor was the concentration of DEG shown in Figure 4. Obviously, the $TiO_2$ nanorods structure is the most obvious, has the largest specific surface area, and was highest when DEG concentration was 7 mol/L. Thus, the optimized condition for ITO-$TiO_2$ and rGO preparation was reaction time of 7 h and DEG concentration of 7 mol/L.
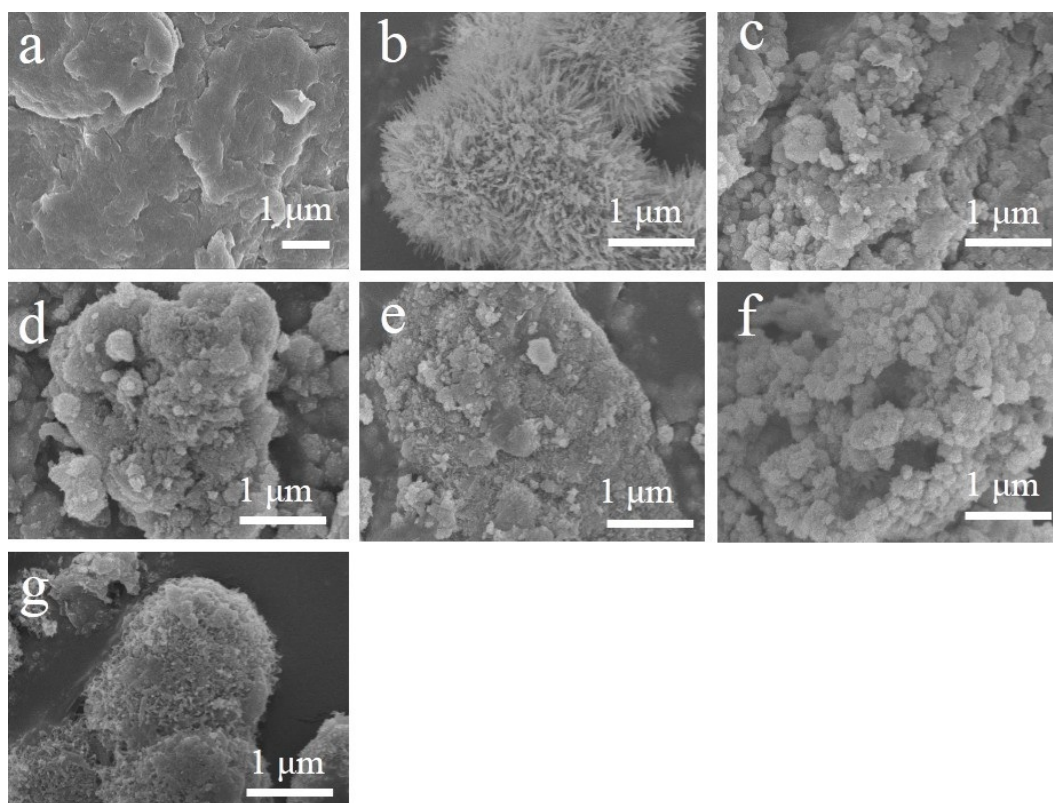
**Figure 3.** Scanning electron microscope (SEM) images of (**a**) rGO, (**b**) TiO$_2$, (**c**) ITO-rGO and TiO$_2$ prepared in 1 h, (**d**) ITO-rGO and TiO$_2$ prepared in 3 h, (**e**) ITO-rGO and TiO$_2$ prepared in 5 h, (**f**) ITO-rGO and TiO$_2$ prepared in 7 h, (**g**) ITO-rGO and TiO$_2$ prepared in 9 h.
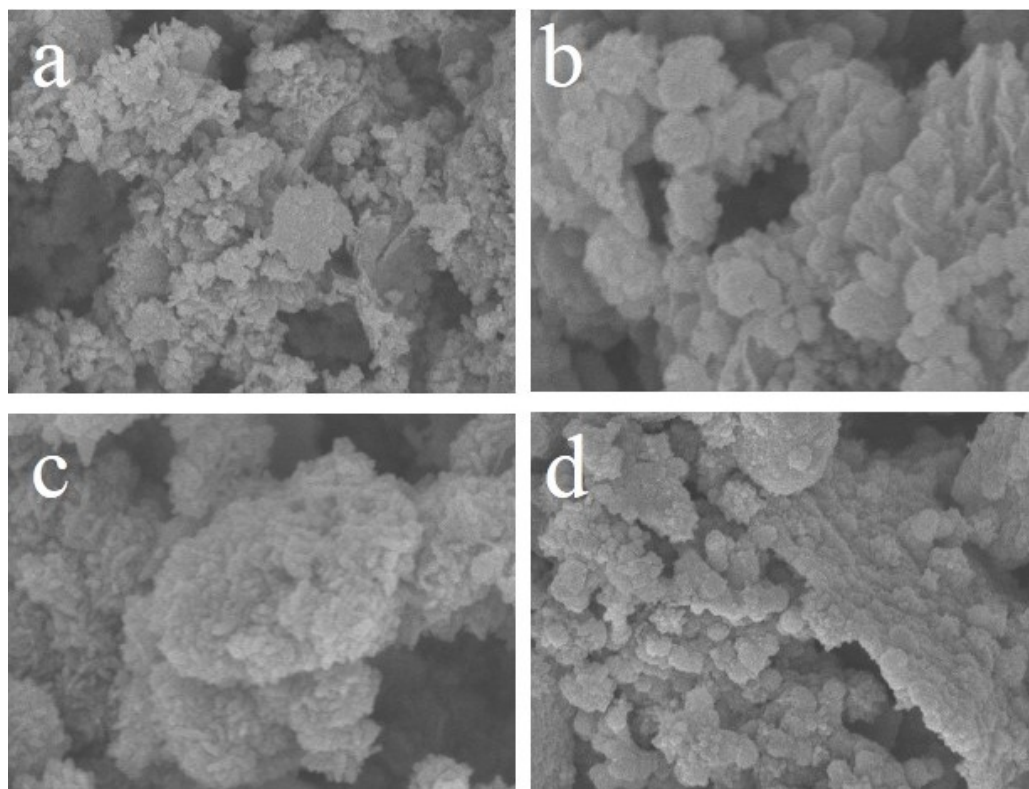


**Figure 4.** SEM images of ITO-rGO and TiO$_2$ prepared in different DEG concentrations: (**a**) 3 mol/L, (**b**) 5 mol/L, (**c**) 7 mol/L, and (**d**) 9 mol/L.

### 2.2.3. TEM

Under such optimized conditions, TEM images of ITO-TiO$_2$ and rGO were detected and results are shown in Figure 5. Figure 5a,b indicates that TiO$_2$ nanorods are grown on the surface of rGO. Additionally, the SAED diffraction patterns of rGO showed that the reduction of GO was relatively complete because of six symmetrically diffraction points that can be clearly observed (Figure 5a inset). Meanwhile, a close-up image of TiO$_2$ nanorods show that the diameter was 20 nm (Figure 5c) and the lattice spacing (d$_{101}$ = 0.35 nm) was observed in TEM images (Figure 5d).
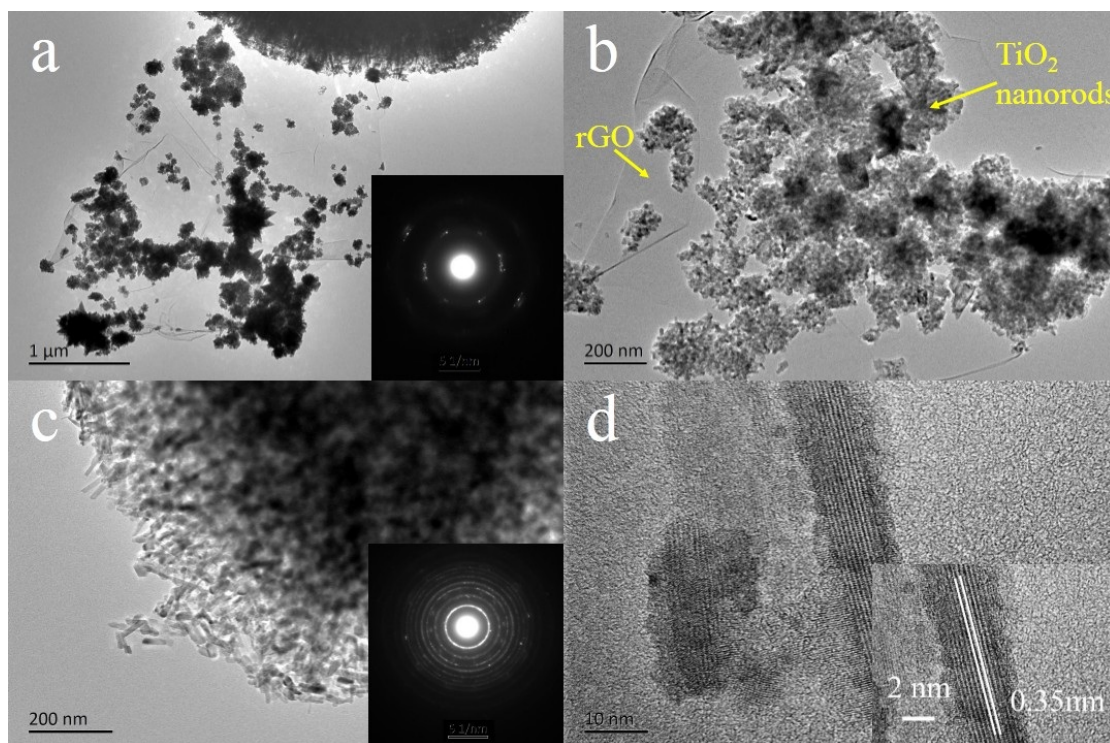


**Figure 5.** Transmission electron microscope (TEM) images and magnification of (**a**,**b**) TiO$_2$ and rGO and (**c**) TiO$_2$, and high-resolution TEM (HRTEM) image of (**d**) TiO$_2$ nanorods (insets are the corresponding SAED diffraction patterns of rGO and TiO$_2$).

### 2.2.4. XPS

To investigate the surface elements of samples, XPS measurements of GO, TiO$_2$, and TiO$_2$ and rGO were carried out (Figure 6). It is obvious that GO contained only C and O elements. However, it also contained K element for TiO$_2$ and TiO$_2$ and rGO samples due to PTO (K$_2$TiO(C$_2$O$_4$)$_2$) (Figure 6a). Figure 6b shows the C1s spectra, which indicated that the binding energies at 284.4 eV (C–C/C=C) and 290.1 eV (O–C=O) were observed [33]. The two main C1s peaks for TiO$_2$ and rGO sharply decreased, confirming the reduction of GO to rGO (Figure 6b). Figure 6c exhibits two main peaks located at 457.9 and 464 eV, which could correspond to Ti 2p3/2 and Ti 2p1/2, respectively [34]. However, these two peaks of TiO$_2$ and rGO shifted towards higher binding energies compared with TiO$_2$. Due to the d–π electron orbital overlap, the binding energy of Ti$^{4+}$ shifted by 0.4 eV [35]. This makes the transmission of electrons more convenient [36] and makes the recombination rate of electron-hole pairs greatly reduced. In Figure 6d the two peaks at 529.1 and 532.6 eV correspond to lattice oxygen (Ti–O) and hydroxyl groups (–OH), respectively.
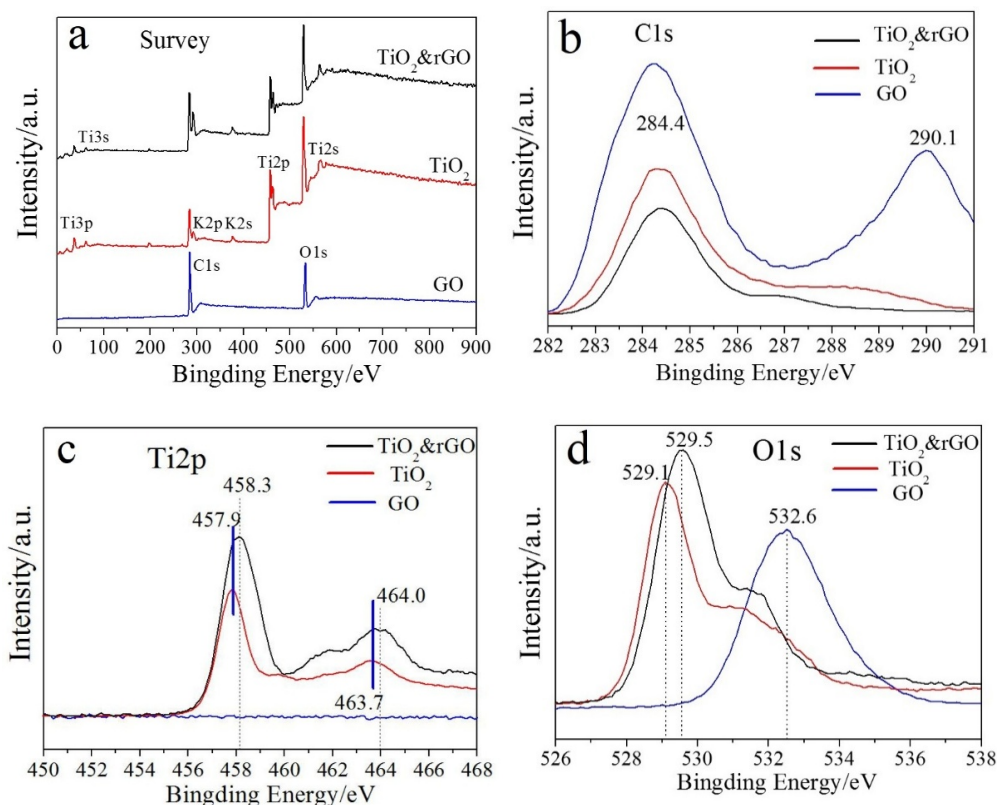
**Figure 6.** X-ray photoelectron spectroscopy (XPS) of (**a**) XPS survey, (**b**) C1s, (**c**) Ti2p, and (**d**) O1s.

### 2.2.5. Raman Spectra

The results of Raman spectra are shown in Figure 7a, four peaks located at frequencies of 149, 400, 515, and 634 $cm^{-1}$ were consistent with the anatase phase of $TiO_2$ with the $D_{4h}19$ ($I4_1/amd$) space group [37]. The intensity of these peaks sharply decrease under the presence of GO for the $TiO_2$ and rGO. It can be determined that $TiO_2$ nanorods were actually grown on the rGO. The weak peak that corresponds to rutile $TiO_2$ was also observed at 230 $cm^{-1}$, and it is also compounded with the results of XRD. In Figure 7b, the D and G bands of GO appear at 1351 and 1602 $cm^{-1}$ [38]. The disorder and defects are generated when the O-rich groups above the rGO are removed which can reduce the recombination of electron-hole pairs [39]. The $I_D/I_G$ means the ratio of the intensity of two peaks which could reflect the number of defects. The $I_D/I_G$ ratio of GO and $TiO_2$ and rGO were 1.12 and 1.14, respectively. This increase shows that the sample has few defects in the complete $sp^2$ hybrid structure. Moreover, the peak intensity of ID for the $TiO_2$ and rGO sample increased compared with GO, showing that the amounts of rGO were reduced.
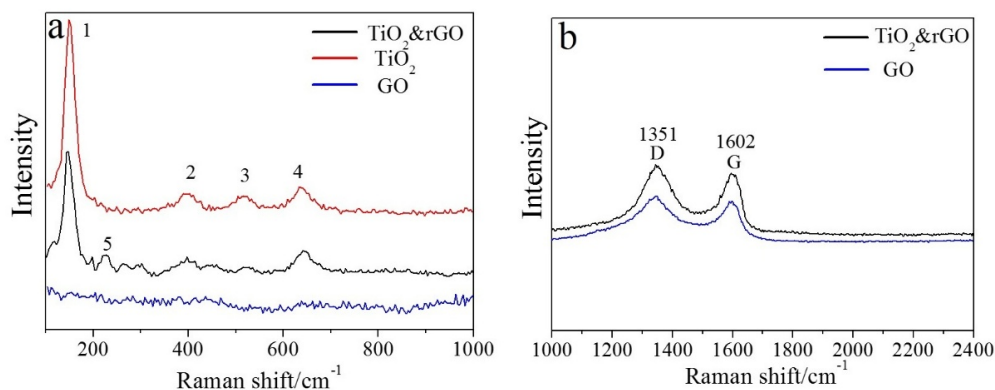


**Figure 7.** Raman spectra of (**a**) $TiO_2$ and (**b**) rGO.

### 2.2.6. FT-IR and UV-Vis Spectra

The reduction of GO to rGO could be further confirmed in FT-IR spectra (Figure S1). The peak of $1730 cm^{-1}$ corresponding to the chemical bond C=O has disappeared for $TiO_2$ and rGO compared with GO, showing that DEG have the ability to reduce GO to rGO. A new peak at $987 cm^{-1}$ appeared because of Ti–O–C bonds between $TiO_2$ and rGO [40,41].

The light-harvesting ability of semiconductors played a vital role in its photocatalytic activity. The absorption spectrum of TIO-$TiO_2$ and rGO was investigated using a diffuse reflectance UV-Vis recording spectrophotometer. We can see that the photocatalysts exhibit similar diffuse reflectance spectra (Figure 8a). The absorption spectrum of TiO-$TiO_2$ and rGO and $TiO_2$ and rGO composite was decreased compared with pure $TiO_2$, which was due to the band gap transition [42]. The band gap could obtain according to Kubelka–Munk equation [43].

$$F(R_\infty) = (1 - R_\infty)^2/2R_\infty \tag{1}$$
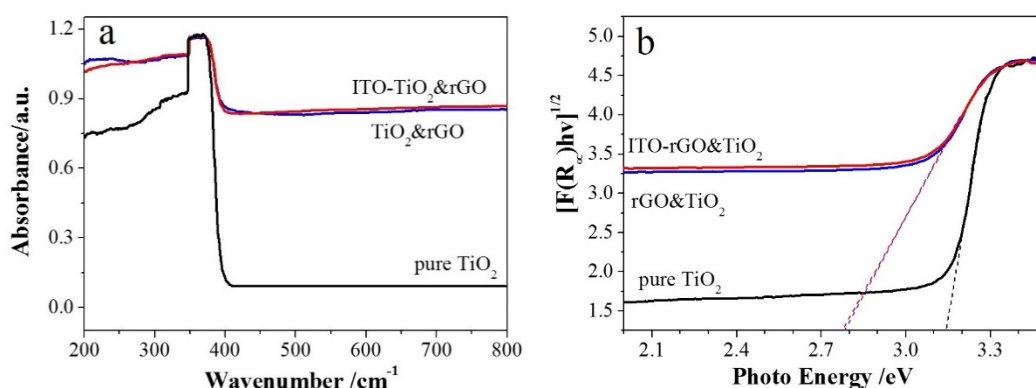
$$F(R_\infty)hv = C_1(hv - E_g)^2 \tag{2}$$



**Figure 8.** (**a**) UV–vis diffuse reflectance spectra (DRS) of the pure $TiO_2$, rGO and $TiO_2$, and ITO-rGO and $TiO_2$, and (**b**) curve of $[F(R_\infty) hv]^{1/2}$ versus photon energy of pure $TiO_2$, rGO and $TiO_2$, and ITO-rGO and $TiO_2$.

As shown in Figure 8b, the band gap of $TiO_2$ was 3.14 eV, and that of ITO-rGO and $TiO_2$ and rGO and $TiO_2$ was about 2.78 and 2.79eV, respectively. The optical band gaps were decreased from 3.14 to 2.78 eV. The addition of rGO resulted in the reduced band gaps and improved absorption and photocatalytic activity of ITO-rGO and $TiO_2$.

### 2.3. Photoelectrical Performance

Figure 9 shows the photocurrent response of ITO-rGO and $TiO_2$ at four on-off cycles, which showed that the photocurrents of electron-hole pairs immediately generated when ITO-rGO and $TiO_2$ electrodes were illuminated. The photocurrent value was increased after coated with rGO. The separated $e^-/h^+$ pairs immediately recombined when light was turned off, which caused the photocurrent to rapidly drop density to almost zero. The reduction in the band gap of ITO-rGO and $TiO_2$ made the transition of the electrons from the valence band to the conducting band easy. Subsequently, the separated electrons migrated to the ITO substrate [44]. Compared to its excellent electrical conductivity, foam nickel has poor light transmission. The ITO glass has a good light transmission property, so that the sample can be illuminated in all directions. The value of the photocurrent is the largest compared with the sample loaded on the foamed nickel. When the light is turned on again, the photocurrent density was not significantly reduced compared to the previous steady photocurrent density value. Therefore, ITO-rGO and $TiO_2$ exhibited stronger photoresponsive property with good reproducibility.
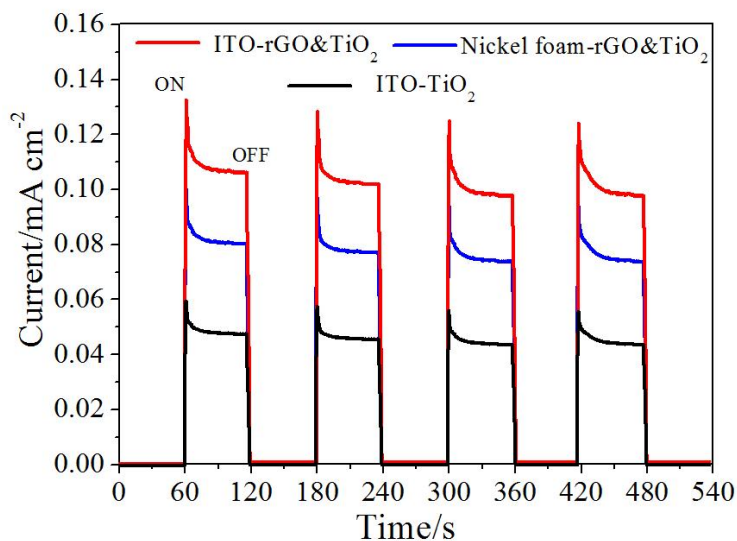
**Figure 9.** Transient photocurrent density of $TiO_2$, Nickel foam-rGO and $TiO_2$, and ITO-rGO and $TiO_2$.

## *2.4. Adsorption and Photocatalytic Properties*

### 2.4.1. Adsorption Kinetics

Figure 10 shows that the adsorption capacity of MB increased with increasing MB concentration. At the beginning, there were more unadsorbed MB molecules that provide a larger adsorption driving force, so the initial adsorption rate was faster. Meanwhile, the Figure 10a results also indicate that the adsorption rate was fast and reached the highest adsorption ability within 30 min. Kinetic studies can use the following equation:

$$\text{Pseudo-first-order-model}: \log(q_e - q_t) = \log q_e - \frac{k_1 t}{2.303} \tag{3}$$

$$\text{Pseudo-second-order-model}: \frac{t}{q_t} = \frac{1}{k_2 q_e^2} + \frac{t}{q_e} \tag{4}$$

As shown in Table S1 and Figure S3, the pseudo-second-order model show a good linearity with higher $R^2$ of 0.9960, and the values of $q_{e,cal}$ and $q_{e,exp}$ were close, which suggests that the dynamic adsorption processes fitted the Pseudo-second-order model for ITO-rGO and $TiO_2$.

Stability and regenerability are an important indicator of evaluation for the adsorbent. As we all know, $TiO_2$ based photocatalysts are usually used under the condition of powders, which leads to difficulty separating the power from the water environment. Thus, the reusable ability of ITO-rGO and $TiO_2$ was investigated using adsorption-desorption experiments (Figure 10b). The adsorption capacity of the sample did not decrease significantly after five cycles showing that ITO-$TiO_2$ and rGO has excellent regeneration and stability ability. The most important is that ITO-$TiO_2$ and rGO was easily recovered from pollution water and thus prevent secondary pollution.

The adsorption capacity of MB increases first and then decreases with the increase of pH value as shown in Figure 10c. As a typical cationic dye, MB is ionized and positively charged, so coulomb rejection occurs between the positive charge on the surface of $TiO_2$ and MB at a relatively low pH range, which results in a relatively low adsorption at pH = 3 for ITO-rGO and $TiO_2$. When pH increased, the electrostatic attraction between the $TiO_2$ and MB increased, leading to an increase in the adsorption capacity [45]. The adsorbability of ITO-rGO and $TiO_2$ reached its maximum when the pH was 9.
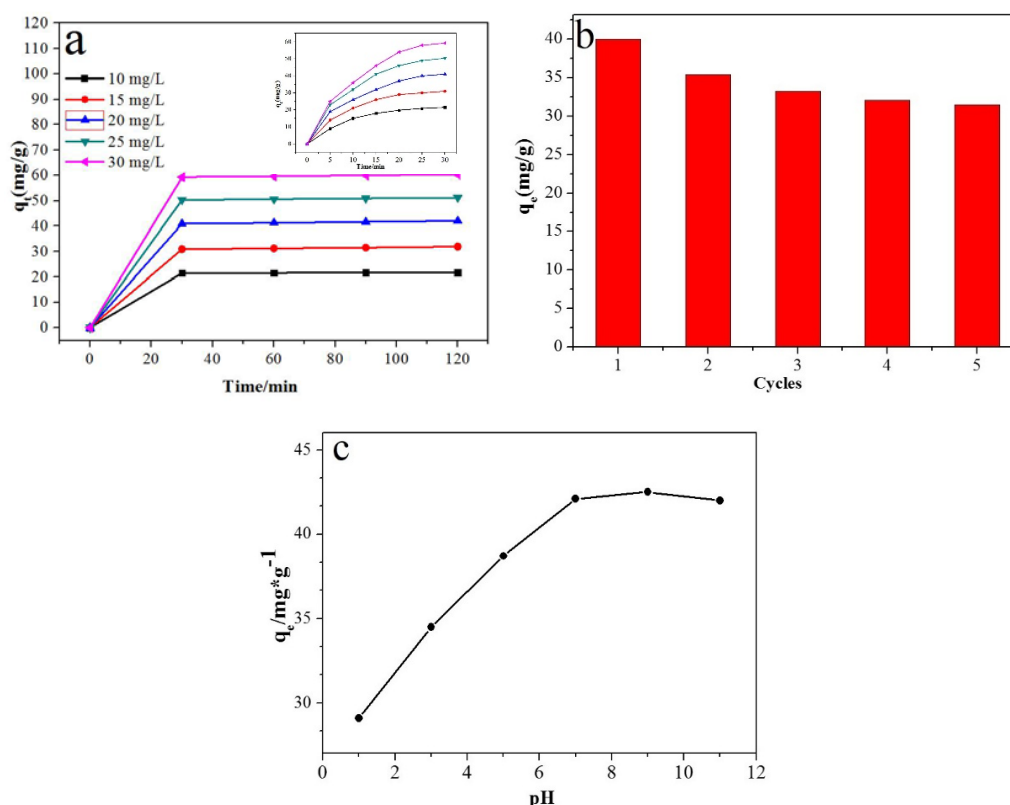
**Figure 10.** (**a**) The adsorption on methylene blue (MB) solution with different initial concentrations (the time range of the inset is 0–30min), (**b**) adsorption capacity of MB on ITO-rGO and TiO$_2$ in five successive cycles, and (**c**) effect of pH value on sample adsorption.

### 2.4.2. Adsorption Thermodynamics

As we all know, thermodynamic studies provide a deeper reference for the adsorption process. The effect of temperature on the adsorption of MB was also investigated. Gibbs free energy can be calculated by the following equation [45]:

$$\Delta G^0 = -RT \ln K_d \tag{5}$$

A high negative value of $\Delta G^0$ represents that the adsorption process is spontaneous. This result is shown in Figure S4 and Table S2, indicating that $\Delta G^0$ values were negative and thus the adsorption process was spontaneous. The equations of enthalpy change and entropy change can be expressed by the following equation [45].

$$\ln K_d = \frac{\Delta S^0}{R} - \frac{\Delta H^0}{RT} \tag{6}$$

### 2.4.3. Adsorption Isotherm

Langmuir isotherms are often applied to the adsorption surface homogenization, and all adsorption sites have the same adsorption affinity. In addition, the Freundlich isotherm model is more focused on homogeneous.

$$\text{Langmuir isotherm}: \frac{C_e}{q_e} = \frac{1}{bq_m} + \frac{C_e}{q_m} \tag{7}$$

$$\text{Freundlich isotherm}: \log q_e = \log K_f + \frac{1}{n}\log C_e \tag{8}$$

Figure S5 shows the application of nonlinear Langmuir and Freundlich isotherms to the MB adsorption on ITO-rGO and TiO$_2$, and the calculated coefficients are listed in Table S3. It can be

seen that the Langmuir isotherm was better for fitting the experimental data with higher regression coefficient ($R^2$) than that of the Freundlich model, which indicates that the active sites on the surface of ITO-rGO and $TiO_2$ were uniform with homogenous adsorption. Furthermore, the essential feature of the Langmuir isotherm can be expressed in terms of a dimensionless constant separation factor ($R_L$) as the following equation:

$$R_L = \frac{1}{1 + bC_0} \tag{9}$$

As we all know, the $R_L$ values show the shape of the isotherm to be either unfavorable ($R_L > 1$), linear ($R_L = 1$), favorable ($0 < R_L < 1$), or irreversible ($R_L = 0$), respectively. The $R_L$ in this study was in the range of 0.166–0.375 for MB adsorption on ITO-rGO and $TiO_2$, which indicated that the shape of isotherm was favorable adsorption.

### 2.4.4. Photocatalytic Activity

Photocatalytic degradation of MB by ITO-rGO and $TiO_2$ were also investigated (Figure 11). It can be seen that in the absence of a photocatalyst (blank), MB is hardly degraded, indicating that MB has high stability under ultraviolet irradiation. However, a great MB degradation was observed in the presence of the photocatalyst of rGO and $TiO_2$ and ITO-rGO and $TiO_2$. Interestedly, the photocatalytic activity of rGO and $TiO_2$ was greatly enhanced after bonding onto the ITO substrate. About 93.40% of MB was decomposed by ITO-rGO and $TiO_2$ within 120 min. The higher photocatalytic degradation of ITO-rGO and $TiO_2$ may be due to the following reasons. Firstly, the electrons from rGO can be collected by the ITO substrate, which lead to improved electron transfer from MB to rGO. Secondly, the electron/hole recombination could be inhibited by ITO-rGO and $TiO_2$ and then extend the holes ($h^+$) existence time.
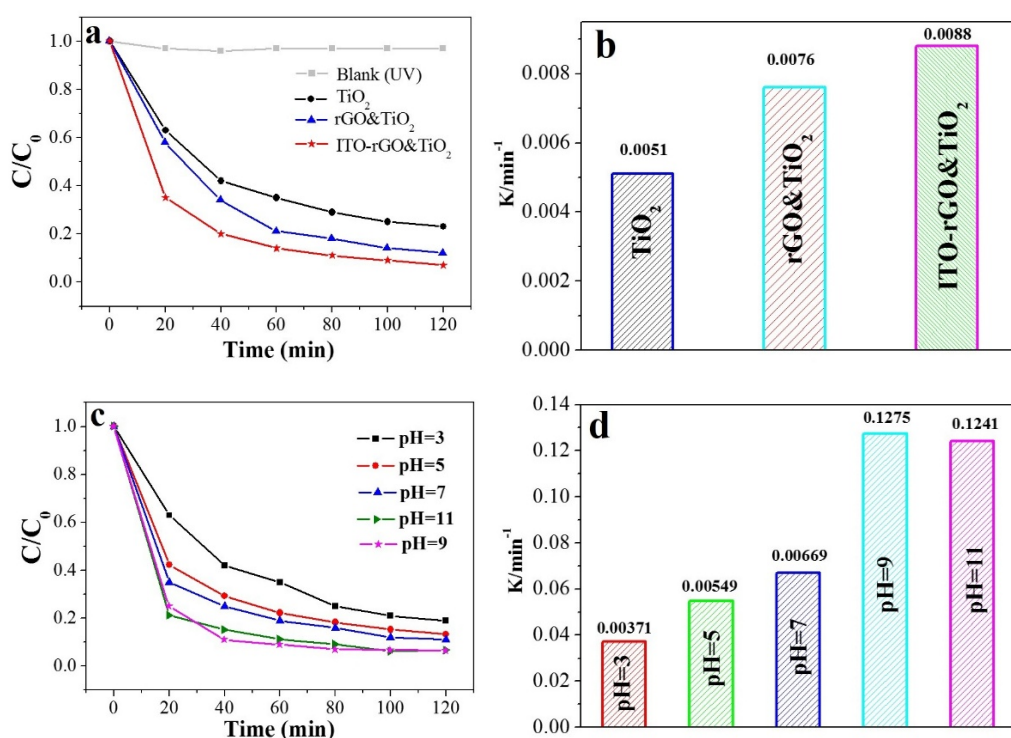


**Figure 11.** Photocatalytic degradation of MB by pure $TiO_2$, rGO and $TiO_2$, and ITO-rGO and $TiO_2$ (**a,c**), and the corresponding first-order rate constant (k) of catalysts in MB decoloring (**b,d**).

An apparent first-order equitation was utilized for comparison of the degradation rate constant of MB on the ITO-rGO and $TiO_2$:

$$\log\left(\frac{C_0}{C}\right) = K_{app}t \tag{10}$$

where $K_{app}$ is the apparent first-order rate constant. As shown in Figure 11b, after modification with rGO and assembly onto ITO, the photocatalytic activity of titanium dioxide is greatly improved. The rate constant of ITO-rGO and $TiO_2$ was 0.0088 $min^{-1}$, which are 1.7 and 1.16 times larger than the rate constants of pure $TiO_2$ and rGO and $TiO_2$, respectively, which further indicates that the photocatalytic activity of $TiO_2$ combined with ITO increases. The most important is that ITO-rGO and $TiO_2$ can be easily recycled and avoid secondary pollution. As we all know, the pH plays an important role in the photocatalytic degradation of contaminants. Thus, the effect of pH on the photodegradation of MB by ITO-rGO and $TiO_2$ was investigated in the pH range from 3 to 11 and the results are shown in Figure 11c,d. According to Equation (10), the pseudo first order rate constants for ITO-rGO and $TiO_2$ were 0.00371, 0.00549, 0.00669, 0.1275, and 0.1241 $cm^{-1}$ in pH solutions of 3, 5, 7, 9, and 11, respectively, showing that ITO-rGO and $TiO_2$ has the highest photocatalytic ability when the pH value was 9, which was due to the strong adsorption of MB on the ITO-rGO and $TiO_2$ at such condition.

Reusability tests and a degradation stability test were also investigated and are shown in Figures S6 and S7. The catalyst was recycled five times to degrade the new undegraded MB solution. The degradation rate did not significantly decrease. In addition, in order to confirm that the MB solution is truly degraded, the degraded MB solution detects the absorbance at fixed time intervals. Figure S7 show that the MB solution is completely degraded.

## 2.5. Mechanism of Degradation

Based on the above systematic studies, the photocatalytic degradation mechanism of MB by ITO-rGO and $TiO_2$ is proposed in Figure 12. Firstly, cationic MB molecules were efficiently adsorbed and enriched on the surface of ITO-rGO and $TiO_2$ due to electrostatic attraction as well as π–π conjugation between MB and rGO. Then, the hydrophilic functional groups on rGO can improve the wettability of ITO-rGO and $TiO_2$ in aqueous solution, and the 3D structure of rGO and $TiO_2$ can shorten the mass transfer distance for the degradation process, which results in enhancement of MB concentration on the surface of ITO-rGO and $TiO_2$. In addition, the typical work functions of $TiO_2$, graphene, and MB are −4.40, −4.42, and −3.60 eV, respectively [42], which showed that the electrons of MB and $TiO_2$ can be accepted by rGO. The adsorbed MB can provide electrons to the graphene (or directly to the photocatalyst) in a photoexcited state (MB*). The electrons transfer through the rGO can be collected by the ITO substrate. ITO can inhibit electron/cloudy recombination, thereby extending the length $(h^+)$ of the time of existence. Finally, MB can be converted to $CO_2$, $H_2O$, and some small molecules. Therefore, the synergy of adsorption-enrichment and photocatalytic reaction was the main mechanism for the high decomposition rate of ITO-rGO and $TiO_2$.
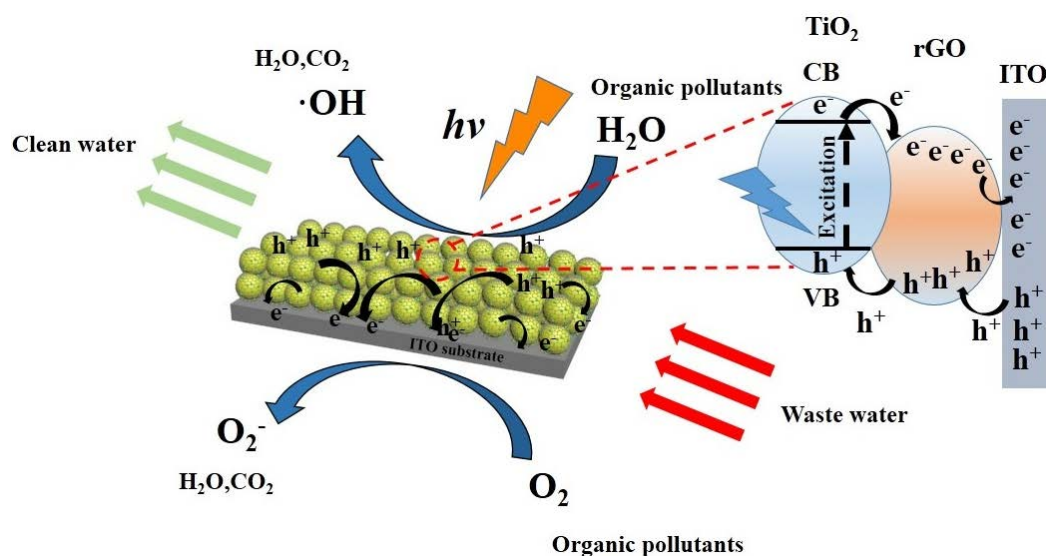


**Figure 12.** Schematic mechanisms of MB decomposition through photodegradation by ITO-rGO and $TiO_2$.

## 3. Experimental Section

### 3.1. Materials

Graphene oxide (GO) was purchased from Shanghai Yuanye Biotechnology Co. Ltd (Shanghai, China). Diethylene glycol (DEG) was obtained from Shanghai Aladdin Biochemical Technology Co. Ltd (Shanghai, China). Tartaric acid was purchased from Shanghai Zhanyun Chemical Co., Ltd (Shanghai, China). Dipotassium Titanium Oxide Dioxalate (PTO) was purchased from Shanghai D&B Biological Science and Technology Co. Ltd (Shanghai, China). Methylene blue (MB) powder was purchased from Sigma Aldrich. The system with the water outlet operated at 18.2 M$\Omega$ (Millipore, Bedford, MA, USA). ITO was purchased from Kaiwei (Zhuhai, China) for the Optoelectronics Technology Co. Ltd.

### 3.2. Preparation of rGO-TiO$_2$

GO powder (0.008 g) was dispersed into water and ultrasonic treated for 3 h at room temperature. The suspensions were then added into a reactor containing a certain amount of DEG (3–9 mol/L), and the total volume of the solution was 80 mL. After adding PTO powder (0.5 g), the suspensions were stirred for 12 h at 60 °C. Polyvinyl pyrrolidone (PVP) (0.5 g) was also added into the solutions and dried at 180 °C for (2–10 h). The powder (rGO and TiO$_2$) was washed with distilled water after the reaction was over. Next, it was dried in a vacuum drying oven at 50 °C and then further calcined in nitrogen at 650 °C for 2 h.

### 3.3. Fabrication of ITO-rGO and TiO$_2$

The powder (rGO and TiO$_2$) were firstly evenly dispersed in 5 mg/mL ethanol. A total of 5 μL of the suspension was dripped on ITO conductive substrate surface. A film formed on the ITO substrate when ethanol evaporated. Six cycles of dropping were carried out. The ITO-rGO and TiO$_2$ was then placed at 450 °C under a nitrogen flow for 1 h.

### 3.4. Characterizations

The morphology of TiO$_2$ powders was identified using an environmental scanning electron microscope (SEM) (JSM-6701F, JEOL, Tokyo, Japan) and transmission electron microscope (TEM) and high-resolution TEM (HRTEM) (JEOL, Tokyo, Japan). X-ray diffractometry (XRD, D8 ADVANCE, Bruker, Karlsruhe, Germany) was employed to characterize the phase structure of the samples. The photocatalytic reaction was carried out in a photochemistry reaction instrument (BL-GHX-V, BILON, Shanghai, China). Raman spectra were recorded on a micro-Raman spectrometer (XploRA PLUS, HORIBA, Beijing, China). X-ray photoelectron spectroscopy (XPS) measurements were conducted by using a Multilab 2000 XPS system (ESCALAB250Xi, ThermoFisher Scientific, Waltham, USA). The Fourier transform infrared (FT-IR) spectra were recorded on an infrared spectrometer (Nicolet5700, Thermo Nicolet, Waltham, USA). Photocurrent measurements were conducted on an electrochemical station (CHI660, Chen Hua, China). A 3 W LED lamp (UVEC-4 II, lamplic, Shenzhen, China) was used as the light source. The UV–vis absorption spectra of the samples were obtained by using a UV–vis spectrophotometer (Cary 100, Agilent Technologies Inc., Beijing, China).

### 3.5. Photoelectrical Performance

In order to test the photoelectrochemical performance of the sample, a three-electrode system that consisted of ITO-rGO and TiO$_2$ (the work electrode), platinum wire (the counter electrode), and Ag/AgCl electrode (the reference electrode) was used. The 3 W UV lamp was used as light source and the responding photocurrent was recorded by electrochemical workstation. The electrolyte was 0.4 mol/L Na$_2$SO$_4$ solution.

*3.6. Photocatalytic Oxidation Reactions of ITO-rGO and TiO₂*

First, 0.01 g of ITO-rGO and TiO₂ was added into a quartz reaction tube with 70 mL MB for the photocatalytic reaction. In order to achieve the adsorption-desorption equilibrium, the suspensions were stirred in the dark for 2 h. The UV absorbance of the MB solution was tested every 20 min. The effect of pH (1–11) and temperature (298, 308, and 318 K) on the removal of MB were also investigated. The amount of MB adsorbed per unit mass can be expressed by this equation

$$q = (C_0 - C_e)V/m. \tag{11}$$

## 4. Conclusions

In this study, rGO and TiO₂ was successfully fabricated by the hydrothermal treatment, which was then assembled onto ITO substrate to form a novel photocatalyst of ITO-rGO and TiO₂. MB can be efficiently enriched on the surface of ITO-rGO and TiO₂ and then easily enter into the 3D structure of rGO and TiO₂. Due to the efficient transfer and separation of photogenerated electrons and holes, rGO can be used as an effective promoter for improving the photocatalytic performance of TiO₂. Meanwhile, ITO substrate can collect electrons from rGO by inhibiting the recombination of electrons. The ITO-rGO and TiO₂ has the advantage of higher adsorption and photocatalytic ability. The most important is that ITO-rGO and TiO₂ can be easily recycled with high stability, which prevents secondary pollution from traditional TiO₂ photocatalysts. Therefore, ITO-rGO and TiO₂ may be a promising photocatalyst in the application of water pollution.

**Supplementary Materials:** The following are available online at http://www.mdpi.com/2073-4344/9/10/848/s1, Figure S1: FTIR of GO, TiO₂ and ITO-rGO and TiO₂, Figure S2: Graph of an ideal photocurrent response, Figure S3: Pseudo-first-order kinetics and pseudo-second-order kinetics of MB adsorption on the ITO-rGO and TiO₂ (prepared by 9 mol/L DEG concentrations at 25 °C), Table S1: Adsorption isotherm parameters for MB adsorption on the TiO₂ and rGO composite, Figure S4: Van't Hoff plot of lnKd vs. 1/T, Table S2: Adsorption thermodynamic parameters for MB adsorption on the TiO₂ and rGO composite, Figure S5: Isotherms of MB adsorption on the ITO-rGO and TiO₂ composite, Table S3: Adsorption isotherm parameters for MB adsorption on the TiO₂ and rGO composite, Figure S6: Degradation ratio of MB on ITO-rGO and TiO₂ in five successive cycles of complete photocatalytic process, Figure. S7: Degradation rate of each interval test sample after the end of the photocatalytic degradation.

**Author Contributions:** Conceptualization, C.G.; Methodology, J.D. and H.P.; Software, S.X., P.X., X.W. and F.L.; Formal analysis, C.G.; Investigation, C.G., Y.X. and J.Y.; Data curation, R.L.; Writing—original draft preparation, C.G.; writing—review and editing, J.D. and H.P; Supervision, J.D. and H.P.

**Conflicts of Interest:** The authors declare no conflict of interest.

## References

1. Sambur, J.B.; Chen, T.; Choudhary, E.; Chen, G.; Nissen, E.J.; Thomas, E.M.; Zou, N.; Chen, P. Sub-particle reaction and photocurrent mapping to optimize catalyst-modified photoanodes. *Nature* **2016**, *530*, 77–80. [CrossRef] [PubMed]

2. Butburee, T.; Bai, Y.; Wang, H.; Chen, H.; Wang, Z.; Liu, G.; Zou, J.; Khemthong, P.; Lu, G.Q.M.; Wang, L. 2D Porous TiO₂ Single-Crystalline Nanostructure Demonstrating High Photo-Electrochemical Water Splitting Performance. *Adv. Mater.* **2018**, *30*, 1705666. [CrossRef] [PubMed]

3. Menny, S.; Snir, D.; Sven, R.; Larissa, G.; Arie, Z. Core/CdS Quantum Dot/Shell Mesoporous Solar Cells with Improved Stability and Efficiency Using an Amorphous TiO₂ Coating. *J. Phys. Chem. C* **2009**, *113*, 3895–3898.

4. Wang, Y.; Gu, L.; Guo, Y.; Li, H.; He, X.; Tsukimoto, S.; Ikuhara, Y.; Wan, L. Rutile-TiO₂ Nanocoating for a High-Rate Li₄Ti₅O1₂ Anode of a Lithium-Ion Battery. *J. Am. Chem. Soc.* **2012**, *134*, 7874–7879. [CrossRef] [PubMed]

5.	Scanlon, D.O.; Dunnill, C.W.; Buckeridge, J.; Shevlin, S.A.; Logsdail, A.J.; Woodley, S.M.; Catlow, C.R.A.; Powell, M.J.; Palgrave, R.G.; Parkin, I.P.; et al. Band alignment of rutile and anatase TiO$_2$. *Nat. Mater.* **2013**, *12*, 798–801. [CrossRef]

6.	Tan, L.; Chai, S.; Mohamed, A.R. Synthesis and Applications of Graphene-Based TiO$_2$ Photocatalysts. *ChemSusChem* **2012**, *5*, 1868–1882. [CrossRef] [PubMed]

7.	Faraldos, M.; Bahamonde, A. Environmental applications of titania-graphene photocatalysts. *Catal. Today* **2017**, *285*, 13–28. [CrossRef]

8.	Zhang, N.; Yang, M.; Liu, S.; Sun, Y.; Xu, Y. Waltzing with the Versatile Platform of Graphene to Synthesize Composite Photocatalysts. *Chem. Rev.* **2015**, *115*, 10307–10377. [CrossRef]

9.	Han, C.; Zhang, N.; Xu, Y. Structural diversity of graphene materials and their multifarious roles in heterogeneous photocatalysis. *Nano Today* **2016**, *11*, 351–372. [CrossRef]

10.	Lu, K.; Chen, Y.; Xin, X.; Xu, Y. Rational utilization of highly conductive, commercial Elicarb graphene to advance the graphene-semiconductor composite photocatalysis. *Appl. Catal. B Environ.* **2018**, *224*, 424–432. [CrossRef]

11.	Geim, A.K. Graphene: Status and Prospects. *Science* **2009**, *324*, 1530–1534. [CrossRef] [PubMed]

12.	Huang, X.; Yin, Z.; Wu, S.; Qi, X.; He, Q.; Zhang, Q.; Yan, Q.; Boey, F.; Zhang, H. Graphene-based materials: Synthesis, characterization, properties, and applications. *Small* **2011**, *7*, 1876–1902. [CrossRef] [PubMed]

13.	Tu, W.; Zhou, Y.; Zou, Z. Versatile Graphene-Promoting Photocatalytic Performance of Semiconductors: Basic Principles, Synthesis, Solar Energy Conversion, and Environmental Applications. *Adv. Funct. Mater.* **2013**, *23*, 4996–5008. [CrossRef]

14.	Xiang, Q.; Yu, J.; Jaroniec, M. Graphene-based semiconductor photocatalysts. *Chem. Soc. Rev.* **2012**, *41*, 782–796. [CrossRef] [PubMed]

15.	Li, Y.; Chen, J.; Huang, L.; Li, C.; Hong, J.; Shi, G. Highly Compressible Macroporous Graphene Monoliths via an Improved Hydrothermal Process. *Adv. Mater.* **2014**, *26*, 4789–4793. [CrossRef] [PubMed]

16.	Low, J.; Yu, J.; Ho, W. Graphene-Based Photocatalysts for CO$_2$ Reduction to Solar Fuel. *J. Phys. Chem. Lett.* **2015**, *6*, 4244–4251. [CrossRef] [PubMed]

17.	Chen, C.; Cai, W.; Long, M.; Zhou, B.; Wu, Y.; Wu, D.; Feng, Y. Synthesis of Visible-Light Responsive Graphene Oxide/TiO$_2$ Composites with p/n Heterojunction. *ACS Nano* **2010**, *4*, 6425–6432. [CrossRef]

18.	Tolosana-Moranchel, Á.; Manassero, A.; Satuf, M.L.; Alfano, O.M.; Casas, J.A.; Bahamonde, A. Influence of TiO$_2$-rGO optical properties on the photocatalytic activity and efficiency to photodegrade an emerging pollutant. *Appl. Catal. B Environ.* **2019**, *246*, 1–11. [CrossRef]

19.	Pu, S.; Zhu, R.; Ma, H.; Deng, D.; Pei, X.; Qi, F.; Chu, W. Facile in-situ design strategy to disperse TiO$_2$ nanoparticles on graphene for the enhanced photocatalytic degradation of rhodamine 6G. *Appl. Catal. B Environ.* **2017**, *218*, 208–219. [CrossRef]

20.	Yang, N.; Zhai, J.; Wang, D.; Chen, Y.; Jiang, L. Two-Dimensional Graphene Bridges Enhanced Photoinduced Charge Transport in Dye-Sensitized Solar Cells. *ACS Nano* **2010**, *4*, 887–894. [CrossRef]

21.	Dai, Y.; Jing, Y.; Zeng, J.; Qi, Q.; Wang, C.; Goldfeld, D.; Xu, C.; Zheng, Y.; Sun, Y. Nanocables composed of anatase nanofibers wrapped in UV-light reduced graphene oxide and their enhancement of photoinduced electron transfer in photoanodes. *J. Mater. Chem.* **2011**, *21*, 18174. [CrossRef]

22.	Huang, Q.; Tian, S.; Zeng, D.; Wang, X.; Song, W.; Li, Y.; Xiao, W.; Xie, C. Enhanced Photocatalytic Activity of Chemically Bonded TiO$_2$/Graphene Composites Based on the Effective Interfacial Charge Transfer through the C-Ti Bond. *ACS Catal.* **2013**, *3*, 1477–1485. [CrossRef]

23.	Li, Z.; Huang, Z.; Guo, W.; Wang, L.; Zheng, L.; Chai, Z.; Shi, W. Enhanced Photocatalytic Removal of Uranium (VI) from Aqueous Solution by Magnetic TiO$_2$/Fe$_3$O$_4$ and Its Graphene Composite. *Environ. Sci. Technol.* **2017**, *51*, 5666–5674. [CrossRef] [PubMed]

24.	Zhang, P.; Xiang, M.; Liu, H.; Yang, C.; Deng, S. Novel Two-Dimensional Magnetic Titanium Carbide for Methylene Blue Removal over a Wide pH Range: Insight into Removal Performance and Mechanism. *ACS Appl. Mater. Interfaces* **2019**, *11*, 24027–24036. [CrossRef] [PubMed]

25.	Le, Q.T.; Nüesch, F.; Rothberg, L.J.; Forsythe, E.W.; Gao, Y. Photoemission study of the interface between phenyl diamine and treated indium–tin–oxide. *Appl. Phys. Lett.* **1999**, *75*, 1357–1359. [CrossRef]

26.	Monamary, A.; Vijayalakshmi, K.; Jereil, S.D. Fe overlayered hybrid TiO$_2$/ITO nanocomposite sensor for enhanced hydrogen sensing at room temperature by novel two step process. *Sens. Actuators B Chem.* **2019**, *287*, 278–289. [CrossRef]

27. Payra, S.; Challagulla, S.; Bobde, Y.; Chakraborty, C.; Ghosh, B.; Roy, S. Probing the photo- and electro-catalytic degradation mechanism of methylene blue dye over ZIF-derived ZnO. *J. Hazard. Mater.* **2019**, *373*, 377–388. [CrossRef]

28. Wolski, L.; Ziolek, M. Insight into pathways of methylene blue degradation with $H_2O_2$ over mono and bimetallic Nb, Zn oxides. *Appl. Catal. B Environ.* **2018**, *224*, 634–647. [CrossRef]

29. Banerjee, S.; Benjwal, P.; Singh, M.; Kar, K.K. Graphene oxide (rGO)-metal oxide ($TiO_2$/$Fe_3O_4$) based nanocomposites for the removal of methylene blue. *Appl. Surf. Sci.* **2018**, *439*, 560–568. [CrossRef]

30. Wu, D.; Yi, M.; Duan, H.; Xu, J.; Wang, Q. Tough $TiO_2$-rGO-PDMAA nanocomposite hydrogel via one-pot UV polymerization and reduction for photodegradation of methylene blue. *Carbon* **2016**, *108*, 394–403. [CrossRef]

31. Ranjan, P.; Agrawal, S.; Sinha, A.; Rao, T.R.; Balakrishnan, J.; Thakur, A.D. A Low-Cost Non-explosive Synthesis of Graphene Oxide for Scalable Applications. *Sci. Rep.* **2018**, 8. [CrossRef] [PubMed]

32. Lv, K.; Fang, S.; Si, L.; Xia, Y.; Ho, W.; Li, M. Fabrication of $TiO_2$ nanorod assembly grafted rGO (rGO@$TiO_2$-NR) hybridized flake-like photocatalyst. *Appl. Surf. Sci.* **2017**, *391*, 218–227. [CrossRef]

33. Dai, Y.; Sun, Y.; Yao, J.; Ling, D.; Wang, Y.; Long, H.; Wang, X.; Lin, B.; Zeng, T.H.; Sun, Y. Graphene-wrapped $TiO_2$ nanofibers with effective interfacial coupling as ultrafast electron transfer bridges in novel photoanodes. *J. Mater. Chem. A* **2014**, *2*, 1060–1067. [CrossRef]

34. Fortes, A.D.; Suard, E.; Knight, K.S. Negative Linear Compressibility and Massive Anisotropic Thermal Expansion in Methanol Monohydrate. *Science* **2011**, *331*, 742–746. [CrossRef] [PubMed]

35. Manga, K.K.; Zhou, Y.; Yan, Y.; Loh, K.P. Multilayer Hybrid Films Consisting of Alternating Graphene and Titania Nanosheets with Ultrafast Electron Transfer and Photoconversion Properties. *Adv. Funct. Mater.* **2009**, *19*, 3638–3643. [CrossRef]

36. Lee, J.S.; You, K.H.; Park, C.B. Highly Photoactive, Low Bandgap $TiO_2$ Nanoparticles Wrapped by Graphene. *Adv. Mater.* **2012**, *24*, 1084–1088. [CrossRef]

37. Lin, Y.P.; Lin, S.Y.; Lee, Y.C.; Chen-Yang, Y.W. High surface area electrospun prickle-like hierarchical anatase $TiO_2$ nanofibers for dye-sensitized solar cell photoanodes. *J. Mater. Chem. A* **2013**, *1*, 9875. [CrossRef]

38. Li, J.; Ishigaki, T.; Sun, X. Anatase, Brookite, and Rutile Nanocrystals via Redox Reactions under Mild Hydrothermal Conditions: Phase-Selective Synthesis and Physicochemical Properties. *J. Phys. Chem. C* **2007**, *111*, 4969–4976. [CrossRef]

39. Yang, J.; Heo, M.; Lee, H.J.; Park, S.; Kim, J.Y.; Shin, H.S. Reduced Graphene Oxide (rGO)-Wrapped Fullerene ($C_{60}$) Wires. *ACS Nano* **2011**, *5*, 8365–8371. [CrossRef]

40. Lui, G.; Liao, J.; Duan, A.; Zhang, Z.; Fowler, M.; Yu, A. Graphene-wrapped hierarchical $TiO_2$ nanoflower composites with enhanced photocatalytic performance. *J. Mater. Chem. A* **2013**, *1*, 12255. [CrossRef]

41. Cao, X.; Tian, G.; Chen, Y.; Zhou, J.; Zhou, W.; Tian, C.; Fu, H. Hierarchical composites of $TiO_2$ nanowire arrays on reduced graphene oxide nanosheets with enhanced photocatalytic hydrogen evolution performance. *J. Mater. Chem. A* **2014**, *2*, 4366–4374. [CrossRef]

42. Lv, K.; Zuo, H.; Sun, J.; Deng, K.; Liu, S.; Li, X.; Wang, D. (Bi, C and N) codoped $TiO_2$ nanoparticles. *J. Hazard. Mater.* **2009**, *161*, 396–401. [CrossRef] [PubMed]

43. Zhang, Y.; Tang, Z.; Fu, X.; Xu, Y. $TiO_2$−Graphene Nanocomposites for Gas-Phase Photocatalytic Degradation of Volatile Aromatic Pollutant: Is $TiO_2$−Graphene Truly Different from Other $TiO_2$−Carbon Composite Materials? *ACS Nano* **2010**, *4*, 7303–7314. [CrossRef] [PubMed]

44. Bell, N.J.; Ng, Y.H.; Du, A.; Coster, H.; Smith, S.C.; Amal, R. Understanding the Enhancement in Photoelectrochemical Properties of Photocatalytically Prepared $TiO_2$-Reduced Graphene Oxide Composite. *J. Phys. Chem. C* **2011**, *115*, 6004–6009. [CrossRef]

45. Aluigi, A.; Rombaldoni, F.; Tonetti, C.; Jannoke, L. Study of Methylene Blue adsorption on keratin nanofibrous membranes. *J. Hazard. Mater.* **2014**, *268*, 156–165. [CrossRef]